J|A|C|S
ARTICLES
Published on Web 07/04/2003

Principles and Features of Single-Scan Two-Dimensional NMR Spectroscopy

Lucio Frydman,*,† Adonis Lupulescu,† and Tali Scherf‡

Contribution from the Departments of Chemical Physics and Chemical Services, Weizmann Institute of Science, 76100 Rehovot, Israel

Received January 27, 2003; Revised Manuscript Received March 25, 2003; E-mail: lucio.frydman@weizmann.ac.il

Abstract: Two-dimensional nuclear magnetic resonance (2D NMR) provides one of the foremost contemporary tools available for the elucidation of molecular structure, function, and dynamics. Execution of a 2D NMR experiment generally involves scanning a series of time-domain signals $S(t_2)$, as a function of a t_1 time variable which undergoes parametric incrementation throughout independent experiments. Very recently, we proposed and demonstrated a general approach whereby this serial mode of data acquisition is parallelized, enabling the acquisition of complete bidimensional NMR data sets via the recording of a single transient. The present paper discusses in more detail various conceptual and experimental aspects of this novel 2D NMR methodology. The basic principles of the approach are reviewed, various homo- and heteronuclear NMR applications are illustrated, and the main features and artifacts affecting the method are derived. Extensions to higher-dimensional experiments are also briefly noted.

Introduction

Despite the decades that have elapsed since its inception, nuclear magnetic resonance (NMR) continues to play an irreplaceable role in determining the structure and dynamics of various physical, chemical, and biological entities at a molecular level.[1,2] Central in endowing NMR with much of its unique potential has been the introduction of two-dimensional (2D) spectroscopy.[3,4] Hundreds of different 2D NMR pulse sequences are today routinely used in almost all areas of experimental Science, ranging from solid-state chemistry and physics, through inorganic, organic, and biochemistry, and onto various areas of *in vivo* experimentation and diagnosis.[5−13]

From a formal standpoint, 2D NMR appears as a natural extension of unidimensional time-domain spectroscopy. Unidimensional measurements collect a signal S as a function of a single acquisition time t; two-dimensional NMR collects the signal as a function of two time variables (t_1,t_2). 1D NMR affords a spectrum $I(\nu)$ after 1D Fourier transformation (FT); 2D NMR provides a spectrum $I(\nu_1,\nu_2)$ after a higher-dimension FT. Yet this parallelism is in fact somewhat deceiving, both in terms of the superior spectral resolution and information content made available by 2D NMR, as well as with regards to the ingenuity required in transforming NMR into a bidimensional form of spectroscopy. Particularly nonintuitive is the implementation of the data acquisition step, because whereas magnetic induction laws allow one to monitor the 1D $S(t)$ signals directly, this is not usually allowed within the 2D time-domain space where $S(t_1,t_2)$ resides. The solution to this sampling problem in 2D NMR—together with much of the insight that later contributed to the success of this form of spectroscopy—was put forward by the seminal contributions of Jeener, Ernst, and coworkers.[3,4] According to the ensuing paradigm of two-dimensional spectroscopy, the actual physical signal induced by the spins in the sample is collected solely as a function of an acquisition time t_2, while the t_1-induced evolution is indirectly monitored via a stepwise incrementation of this time parameter within the NMR pulse sequence. Although of a reliability beyond arguments, the indirect t_1-encoding that this classical 2D NMR protocol proposes is associated to one potential drawback: given that numerous t_1 increments are required for properly characterizing the initial evolution frequencies, and that

† Department of Chemical Physics.
‡ Department of Chemical Services.

(1) Abbreviations: 2D NMR, two-dimensional nuclear magnetic resonance; FT, Fourier transform; MRI, magnetic resonance imaging; EPI, echo-planar imaging; EPSI, echo-planar spectroscopic imaging; COSY, correlated spectroscopy; TOCSY, total correlation spectroscopy; INEPT, insensitive nuclei enhanced by polarization transfer; HSQC, heteronuclear single-quantum correlation; TPPI, time-proportional phase incrementation; S/N, signal-to-noise ratio.

(2) *Encyclopedia of NMR*; Grant, D. M., Harris, R. K., Eds.; J. Wiley & Sons: Chichester, 1996.
(3) Jeener, J. Ampere International Summer School II, Basko Polje, Yugoslavia, September 1971.
(4) Aue, W. P.; Bartholdi, E.; Ernst, R. R. *J. Chem. Phys.* **1976**, *64*, 2229.
(5) Wuthrich, K. *NMR of Proteins and Nucleic Acids*; J. Wiley & Sons: New York, 1986.
(6) Ernst, R. R.; Bodenhausen, G.; Wokaun, A. *Principles of Nuclear Magnetic Resonance in One and Two Dimensions*; Clarendon: Oxford, 1987.
(7) Kessler, H.; Gehrke, M.; Griesinger, C. *Angew. Chem., Int. Ed. Engl.* **1988**, *27*, 490.
(8) Schmidt-Rohr, K.; Spiess, H. W. *Multidimensional Solid-State NMR and Polymers*; Academic Press: London, 1994.
(9) Sanders, J. K. M.; Hunter, B. K. *Modern NMR Spectroscopy: A Guide for Chemists*; Oxford University Press: Oxford, 1994.
(10) Cavanagh, J.; Fairbrother, W. J.; Palmer, A. G.; Skelton, N. J. *Protein NMR Spectroscopy: Principles and Practice*; Academic Press: San Diego, 1996.
(11) Brown, M. A.; Semelka, R. C. *MRI: Basic Principles and Applications*; Wiley-Liss: New York, 1999.
(12) Levitt, M. *Spin Dynamics*; John Wiley & Sons: New York, 2001.
(13) Buxton, R. B. *An Introduction to Functional MRI: Principles and Techniques*; Cambridge University Press: Cambridge, 2001.

10.1021/ja030055b CCC: $25.00

each one of these increments is associated with an independent signal acquisition, 2D NMR will require the collection of several independent scans even if dealing with systems possessing no signal-to-noise ratio (S/N) limitations.

Long acquisition times proved particularly confining in what eventually became the most widespread form taken by bidimensional NMR spectroscopy: 2D magnetic resonance imaging (MRI).[11,13] The unparalleled flexibility with which the interactions defining 2D MRI—given in essence by artificial gradient-based frequency shifts—can be introduced and removed, enabled the eventual development of alternatives which bypass the acquisition time limitations of traditional 2D NMR.[14−16] Foremost among these ultrafast alternatives is echo-planar imaging (EPI), a multidimensional MRI technique proposed by Mansfield which encodes the spins' physical location within a single scan by successively switching on and off the various magnetic field gradients involved in the correlation.[14,17] Only in very rare instances, however, dealing mainly with interactions that can be manipulated and reversed with nearly 100% efficiencies, could the principles underlying this imaging methodology be extended to purely spectroscopic NMR applications. Examples of these involve single-scan *J*-resolved and quadrupole-resolved acquisitions,[18−20] experiments which, although basic, do not find widespread use within modern 2D NMR.

The main impediment preventing the extension of ultrafast EPI scanning ideas to spectroscopy experiments lies in our inability to swiftly control or reverse the spin interactions that are normally involved in 2D NMR. Indeed, neither the coupling nor the relaxation-driven transfer processes among spin coherences or populations underlying much of modern 2D spectroscopy (TOCSY, COSY, NOESY, MQ NMR[5−10,12]) can be suspended or reversed the numerous times required by EPI-type protocols. Very recently, however, we demonstrated an alternative route to the ultrafast acquisition of 2D NMR spectra, based on replacing the usual time encoding of the signals by an equivalent spatial encoding of the spin evolution frequencies operating along the experiment's indirect domain.[21] This spatial encoding of the interactions is a procedure that unlike the serial incrementation of t_1 values hitherto used in 2D NMR can be parallelized, making it possible to collect the equivalent of complete $S(t_1,t_2)$ data sets within a single scan. Because the nature of the interactions being correlated or of the transfer processes taking place during the mixing portion of the sequence is not relevant to this parallelization of 2D NMR experiments, the methodology becomes of a general nature. Figure 1 illustrates the potential of this new type of acquisition mode with 2D NMR TOCSY spectra collected for simple dipeptides within a fraction of a second; the features evidenced by these spectra are as expected.

The purpose of the present Article is to present an expanded description about the basic principles, potential, and features of this new ultrafast 2D NMR methodology. For the sake of clarity, we decided to partition this account into three main sections. In the first one, the basic principles that enable the gradient-assisted acquisition of 2D NMR spectra in a single scan and the various stages that make up the realization of these experiments are described in simple pictorial terms. Although only qualitative, it is shown that these principles can provide a physical picture of the unusual way peaks are generated in such spatially encoded experiments. A results-based section then follows, where the methodology is illustrated with a variety of single-scan 2D NMR sequences, as well as with a potential extension to higher dimensions. We conclude by presenting a deeper discussion on various basic aspects of the methodology and by putting forward a number of further potential improvements and extensions.

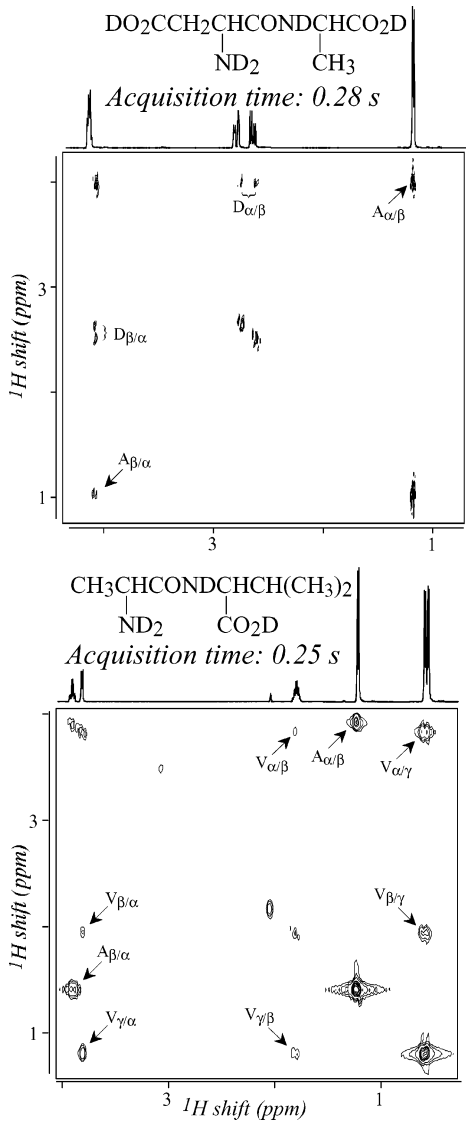

Figure 1. 2D phase-sensitive (top) and magnitude (bottom) TOCSY ^{1}H NMR spectra collected within a single scan on AspAla and AlaVal samples dissolved in D_2O, using a 1.5 s water presaturation pulse, ca. 100 ms long DIPSI-based mixing periods, and the protocol described in the present study. Intraresidue cross-peak are assigned by the arrows; also shown on top of the 2D contours are the corresponding unidimensional traces. Each of the experiments, involving 58 t_1 "points" (slices) and 256 t_2 "points" (echoes), was carried out on a Varian INOVA 500 MHz NMR spectrometer using an inverse probehead incorporating a 65 G/cm *z*-gradient. Further experimental details on the single-scan protocol are discussed in the text.

(14) Mansfield, P. *J. Phys. C: Solid State Phys.* **1977**, *10*, 55.
(15) Frahm, J.; Haase, A.; Matthaei, D. *Magn. Reson. Med.* **1986**, *3*, 321.
(16) Haase, A. *Magn. Reson. Med.* **1990**, *13*, 77.
(17) Stehling, M. K.; Turner, R.; Mansfield, P. *Science* **1991**, *254*, 43.
(18) Bax, A.; Mehlkoff, A. F.; Smidt, J. *J. Magn. Reson.* **1980**, *40*, 213.
(19) Frydman, L.; Peng, J. *Chem. Phys. Lett.* **1994**, *220*, 371.
(20) Blumler, P.; Jansen, J.; Blumich, B. *Solid State Nucl. Magn. Reson.* **1994**, *3*, 237.
(21) Frydman, L.; Scherf, T.; Lupulescu, A. *Proc. Natl. Acad. Sci. U.S.A.* **2002**, *99*, 15858.

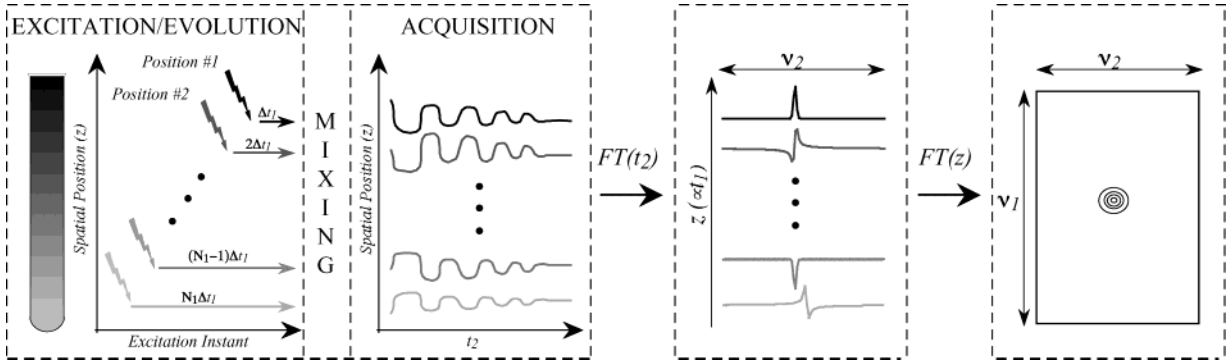

Figure 2. Simplified scheme depicting the application of spatially heterogeneous excitation and detection schemes, toward the acquisition of multidimensional NMR data within a single scan. The excitation that triggers the initial spin evolution is assumed to affect spins in different positions within the sample at a series of incremented times (left panel). This creates a spatial-encoding of the initial t_1 evolution period, which is then monitored as a function of t_2 via the spatially resolved acquisition of the NMR signal. Following FT of the signals against the t_2 and spatial variables, this strategy allows one to retrieve a complete 2D NMR spectrum within a single scan (right panel).

Methods

Principles of Single-Scan 2D NMR Spectroscopy. The canonical 2D NMR scheme

$$\text{preparation/excitation} - \text{evolution}\ (t_1) - \text{mixing} - \text{detection}\ (t_2) \quad (1)$$

involving common and sequential evolution, mixing, and acquisition periods for all spins throughout the sample, is not easily amenable to implementation within a single scan. The ultrafast 2D NMR methodology that we propose bypasses this limitation by partitioning the sample into a series of independent subensembles, each of them characterized by an individual t_1 evolution. Such partitioning could be done, for instance, by applying a time-incremented series of N_1 spatially selective excitation sequences throughout the sample (Figure 2). A common mixing period followed by the observation of the independent signals generated by each member of this set can then enable the simultaneous acquisition of a complete conventional-type 2D NMR data set. The overall acquisition scheme would then be summarized as

$$\left[\begin{array}{c}\text{spatially selective}\\ \text{preparation/excitation}\end{array}\right]_{N_1} - \begin{array}{c}\text{position-dependent}\\ \text{evolution}\ (t_1)\end{array} - \begin{array}{c}\text{position-independent}\\ \text{mixing}\end{array} - \begin{array}{c}\text{spatially resolved}\\ \text{acquisition}\ (t_2)\end{array} \quad (2)$$

Although evidently more complex than the original 2D NMR scheme in eq 1, this partitioning of the sample offers the potential to collect the complete bidimensional data set within a single scan. This, of course, provided that methods are devised for endowing the various N_1 subensembles with individual t_1 evolution times, and then for monitoring the signals that these generate independently and within a single transient.

It is possible to propose several alternatives for achieving the spatially heterogeneous evolution and detection processes described in eq 2. Out of these alternatives, we concentrate for simplicity on those illustrated in Figure 3 for the excitation process, and in Figure 4 for the acquisition process. It appears that when dealing with a conventional isotropic sample, the simplest route to achieve a heterogeneous set of evolution times is by imposing an auxiliary gradient on top of the homogeneous external magnetic field B_o. This, in turn, enables a sequential excitation of the spins, based on the use of a train of frequency-shifted selective radio frequency (rf) pulses (Figure 3A). Spacing these pulses in equal time steps as well as in constant offset increments allows one to achieve the equi-spaced evolution progression envisioned in Figure 2. Using a gradient-based scheme opens in turn the question of how to impart on successively excited spin-packets an evolution phase that reflects solely the internal coupling frequencies, but not the frequencies defined by

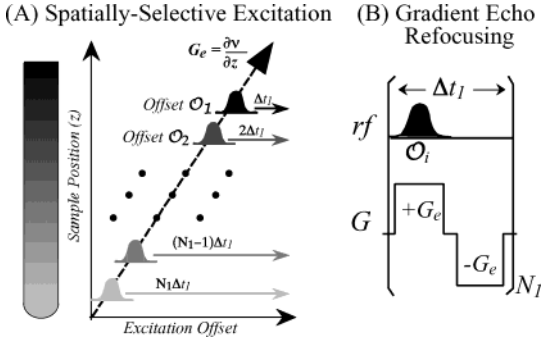

Figure 3. (A) A train of frequency-shifted rf excitation pulses applied while in the presence of a magnetic field gradient can be used to achieve an incremented evolution (t_1) of spins throughout the sample. If a constant offset increment $\Delta O = |O_{i+1} - O_i|$ is used, the constant Δz spacing assumed by the protocol in Figure 2 is achieved. (B) The train of frequency-shifted pulses needs to be applied in combination with synchronized reversals in the sign of the field gradient (gradient echoes) if an evolution that is solely dictated by the internal spin evolution frequencies is to be achieved.

the artificial gradient. This goal can be achieved if following the action of each selective pulse, the $+G_e$ gradient employed to implement the spatially heterogeneous excitation is reversed via an opposite gradient of amplitude $-G_e$ (Figure 3B). Assuming that gradients in this pair are applied for equal time lengths T_p (e.g., the rf pulse duration), we found that this will result in a gradient echo where any dephasing that may have affected hitherto excited magnetizations becomes compensated.

The next aim is to monitor the signals originating from these individually excited slices, after they have been subject to the mixing process. This spatially resolved detection of the signal as a function of t_2 amounts to a hybrid spectroscopic/imaging experiment,[22,23] an acquisition that can be implemented within a single scan using a number of alternatives.[24,25] In particular, during this initial stage of the methodology's development, the echo-planar spectroscopic imaging technique developed by Mansfield (EPSI, Figure 4) was adopted toward this end.[26] NMR signals are collected throughout an EPSI experiment from spins that evolve while subject to an alternating field gradient.[26−28]

(22) Brown, T.; Kincaid, B.; Ugurbil, K. *Proc. Natl. Acad. Sci. U.S.A.* **1982**, *79*, 3523.
(23) Pykett, I.; Rosen, B. *Radiology* **1983**, *149*,
(24) Callaghan, P. T. *Principles of Nuclear Magnetic Resonance Microscopy*; Oxford University Press: Oxford, 1991.
(25) Blumich, B. *NMR Imaging of Materials*; Oxford University Press: Oxford, 2000.
(26) Mansfield, P. *Magn. Reson. Med.* **1984**, *1*, 370.
(27) Matsui, S.; Sekihara, K.; Kohno, H. *J. Am. Chem. Soc.* **1985**, *107*, 2817.
(28) Guilfoyle, D. N.; Blamire, A.; Chapman, B.; Ordidge, R. J.; Mansfield, P. *Magn. Reson. Med.* **1989**, *10*, 282.

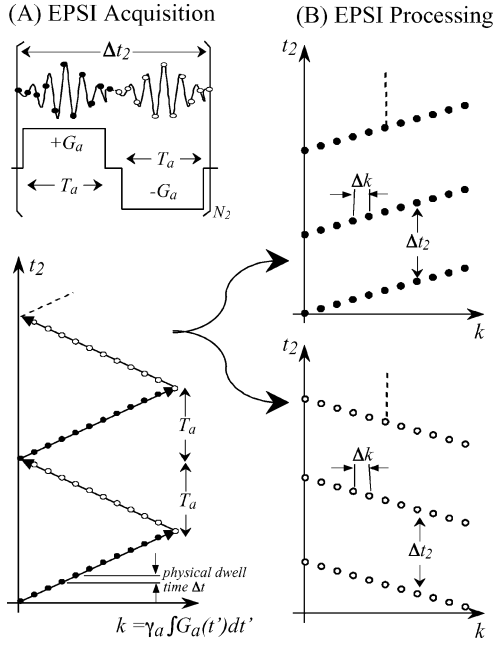

Figure 4. (A) Basics of the echo-planar spectroscopic imaging (EPSI) protocol employed throughout the present work to detect the spins' frequencies in a spatially resolved fashion. Signals are monitored as a function of k and t_2 variables; ○ and ● dots symbolize the coordinates of points digitized during the course of positive and negative acquisition gradients. Such a gradient echo module is then repeated N_2 times, with N_2 defining the number of effective points along t_2. (B) As data stemming from an EPSI scheme employing a constant rate of digitization are not arrayed within a regular grid ready to be 2D FT, points need to be sorted out into two independent bidimensional data sets that are then individually processed. Both 2D data sets can then be co-added for the sake of improving the overall S/N.

This leads to signals becoming simultaneously encoded according to the spins' spatial positions, as well as to their internal evolution frequencies. Such encoding can be summarized by an evolution phase $\phi = k\cdot z + t_2\cdot\nu_2$, where $k = \int_0^{t_2}\gamma_a G_a(t)\,dt$ is a gradient-related wavenumber encoding position, and t_2 reflects the extent of the free evolution and encodes the internal frequency. Evolution while in the presence of an oscillating $\pm G_a$ gradient can then be represented by a "zig-zagging" trajectory throughout the (k,t_2)-space, which is to be digitized with a sufficiently short dwell time to characterize both the k- and the t_2-behavior in a continuous fashion (Figure 4A). Processing such an EPSI set into a spatially resolved 2D NMR spectrum requires transforming the signal contained in these points against the two extraction variables (k,t_2). These points do not appear distributed over the regular 2D grid that is needed for carrying out a fast FT, a complication that is usually resolved by implementing a separation procedure like the one illustrated in Figure 4B prior to the transform. Separating interleaved data sets in such fashion provides two $S(k,t_2)$ signals displaying a regular spacing between consecutive points, thus being ready for the fast FT.

Fourier Relations in Spatially Encoded 2D NMR Spectroscopy. Having introduced a basic strategy for the full multiplexing of 2D NMR via spatial heterogeneities, we find that it is convenient to discuss next the basic Fourier relations and data processing details of such a methodology. Although somewhat abstract, such arguments prove valuable toward understanding how peaks are generated during the course of these single-scan experiments. As introduced in the preceding section, signals in the ultrafast 2D NMR experiment appear collected as a function of two extraction variables: k, encoding the spins' spatial positions, and t_2, encoding their internal frequencies ν_2 at the time of the acquisition. A third additional modulation factor $\exp(i\nu_1 t_1)$, depending on the extent of the encoding experienced by the spins prior to the mixing period, will also affect parametrically the acquired $S(k,t_2)$ signal. All of this can be summarized as

$$S(k,t_2) = \int_{\nu_1}\int_{\nu_2}\int_z P(\nu_1,\nu_2,z)e^{i\nu_1 t_1}e^{i\nu_2 t_2}e^{ikz}\,d\nu_1\,d\nu_2\,dz \qquad (3)$$

The $P(\nu_1,\nu_2,z)$ distribution in this equation denotes the joint probability that spins in the sample placed at a particular coordinate Z will have evolved with a given frequency Ω_1 during t_1 and with a subsequent frequency Ω_2 during t_2. As the sample under consideration can be assumed to be of a homogeneous spatial composition, $P(\nu_1,\nu_2,z)$ can be safely rewritten as $\rho(z)\cdot I(\nu_1,\nu_2)$, where $\rho(z)$ denotes the shape of the sample that was excited, and $I(\nu_1,\nu_2)$ denotes the 2D NMR spectrum being sought. $\rho(z)$ is the only function in the integrand of eq 3 that is explicitly z-dependent and is, in fact, a constant ρ_o throughout the active sample volume. A FT of $S(k,t_2)$ along the k-domain will thus afford a kernel that is simply

$$S(z,t_2) = \rho_o\int_{\nu_1}\int_{\nu_2} I(\nu_1,\nu_2)e^{i\nu_1 t_1}e^{i\nu_2 t_2}\,d\nu_1\,d\nu_2 \qquad (4)$$

Care needs to be taken at this point of the fact that the t_1 evolution time was also varied as a function of z. In particular if—as illustrated in Figure 2 and actually done throughout the experiments that will be here described—t_1 was varied linearly with z, the explicit introduction of t_1's spatial dependence results in

$$S(z,t_2) = \rho_o\int_{\nu_1}\int_{\nu_2} I(\nu_1,\nu_2)e^{i\nu_1[C(z-z_o)]}e^{i\nu_2 t_2}\,d\nu_1\,d\nu_2 \qquad (5)$$

It is then clear that a 2D FT of $S(z,t_2)$ with respect to (z,t_2) can provide the 2D NMR spectrum $I(\nu_1,\nu_2)$ correlating evolution and acquisition frequencies, as initially sought.

An odd feature of this analysis is its reliance on a FT against k to define the z spatial location of the spins, followed by a FT against z to define the spins' ν_1 evolution frequencies. Because the FT is a self-reciprocal operation, this would indicate that, under the $t_1 \propto z$ assumption, no FT of the data along the k-axis is needed altogether. Indeed, spectra shown throughout this work were obtained by subjecting the data arising from the EPSI preprocessing manipulations depicted in Figure 4 solely to a FT along the t_2 axis. This nonconventional processing stems from the fact that, in this kind of experiment, peak positions along the indirect domain are not defined via the Fourier analysis of a time-evolving coherence, but via the displacement observed in k-space for the position of an echo created by interfering magnetizations from different slices. A graphical depiction of this feature is illustrated in Figure 5, which analyzes the fate of magnetizations throughout a portion of an ultrafast acquisition assuming a simplified "five-slices" sample. The initial excitation segment of the sequence affects successively the various slices and imposes on them a spatial-encoding; yet this encoding will only reflect the initial Ω_1 internal evolution frequency, because the effects of the auxiliary G_e are being compensated by our reliance on gradient echoes. The extent of the ensuing evolution can therefore be described for a particular site by a "winding" of its magnetization through the sample, with a pitch dictated by $\exp[iC\Omega_1(z-z_o)]$. This spatial winding is then preserved as either a phase- or an amplitude-modulation throughout the mixing period, with the result that the overall signal available for detection at the beginning of the acquisition will in general be null. At this point, however, a gradient is applied on the sample, whose spatial $\exp[i\gamma_a(\int_0^t G_a(t')\,dt')z]$ dependence is capable of unwinding the initial spiral of magnetizations. Such unwinding will lead to a constructive interference among the spin-packets corresponding to different slices whenever $k = \gamma_a\int_0^t G_a(t')\,dt' = -C\Omega_1$, thus decoding the initial evolution frequency that was active during t_1 via the location of an echo along the k-axis. This echo makes up the "peak" that will be observed along the indirect domain, whose further evolution as a function of the time t_2 is then monitored by successive dephasing and

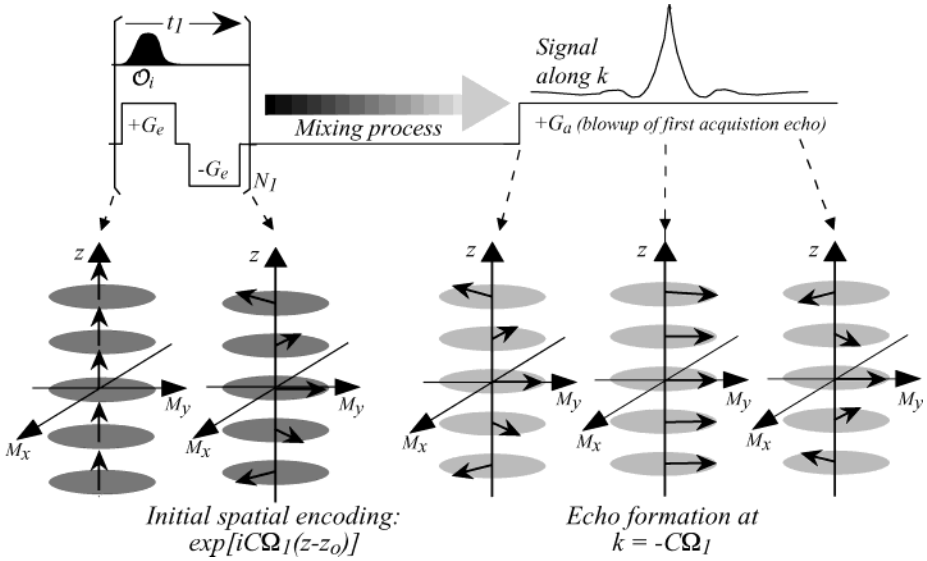

Figure 5. Simplified cartoon describing the origin of peaks along the indirect dimension of ultrafast 2D NMR experiments. The heterogeneous nature of the t_1 evolution leads to an encoding of the internal precession frequency Ω_1 along the z axis (second panel from left); this spiral of spin-packets is subsequently unwound by an acquisition gradient G_a possessing an identical z spatial dependence. The coherent addition of spin-packets thus leads to a sharp echo along the k coordinate whose position reveals the extent of Ω_1 encoding prior to the mixing process—in essence, the spectrum along the indirect dimension. Such "peak" formation is only illustrated here for a portion of the first acquisition gradient echo; the phase encoding gained by this echo peak during the course of the N_2 gradient-reversals occurring as a function of t_2 provides a conventional route to measure the Ω_2 frequencies active during the acquisition.

rephasing processes driven by changes in the sign of G_a. Hence, no additional k-axis Fourier transformation becomes necessary to decode the indirect evolution frequencies active during t_1.

Although a more mathematical description of various features involved in this echo formation is given in the Discussion section below, these simple Fourier arguments enable a derivation of basic Nyquist criteria for the new acquisition scheme. Denoting T_a as the duration during which $\pm G_a$ gradients are applied and Δt as the actual physical dwell time (Figure 4A) leads to $N_k = T_a/\Delta t$ complex points being collected along the k-axis. Assuming then that the $\pm G_a$ cycle is repeated N_2 times results in a $2T_aN_2$ total digitization time for the experiment and in $2N_2N_k$ complex points being collected overall. Points following the data separation procedure will be spaced along t_2 by $2T_a$ intervals, leading to $SW_2 = (2T_a)^{-1}$ spectral widths along the direct domain. The maximum range that under such conditions will be scanned along the k/ν_1-axis is $k_{max} = \gamma_a G_a T_a$, which will in turn enable peaks to be accommodated over a $SW_1 = |k_{max}/C|$ spread along the indirect domain. As defined in eq 5, the constant C is given by the ratio between the extent of t_1 evolution and the degree of spatial z encoding: $C = \Delta t_1/\Delta z = \Delta t_1/[\Delta O/\gamma_e G_e]$, Δt_1 being the time between one excitation pulse and the next, $\gamma_e G_e$ the gradient's strength during excitation, and $\Delta O = |O_{i+1} - O_i|$ the constant increment used to offset the selective excitation pulses. Under the idealized scheme in Figure 3, $\Delta t_1 \approx 2T_p$, twice the selective pulses' duration; C is then $2T_p\gamma_e G_e/\Delta O$, and the overall indirect spectral width becomes (in frequency units) $SW_1 = |\Delta O(\gamma G_a T_a/2\gamma_e G_e T_p)|$. These expressions for SW_1 and SW_2 are of practical quantitative use, provided that corrections are made for the gradients' nonidealities.[29]

Results

Having discussed the basic principles of ultrafast 2D NMR and the origin of peaks in these experiments, we survey next a series of model experimental tests that were assayed using this methodology. Figure 6 illustrates a basic 2D ^{1}H NMR acquisition on an *n*-butyl chloride sample, using a 2D test pulse sequence that actually involves no mixing process. Identical frequencies have here been active throughout the evolution and acquisition times, and only diagonal peaks result. As in all ultrafast experiments that will be later reported, these data were collected as a unidimensional set, which when magnified appears to be composed by a series of 1D indirect-domain NMR spectra (Figure 6A). This is a reflection of the method's built-in capability to FT the signal that was encoded during t_1, via the G_a gradient defining the k-axis. Processing continues with the assembling of the $S(k,t_2)$ 2D data set (Figure 6B) followed by the separation of the points corresponding to alternate $+G_a/-G_a$ acquisitions, whose onward processing is carried out independently (Figure 6C). A recursive artifact that we observe in these (and in other) ultrafast 2D NMR data sets consists of a "tilting" of the k-space peaks, when followed as a function of time t_2. This artifact grows as the intensity and/or duration of the gradients used in the experiment increases, and numerical simulations further detailed below suggest that it arises from a small weakening in the gradients' absolute value as a function of the acquisition time t_2 ("gradient drooping"). Rather than compensating for this effect instrumentally, we decided to correct it via a numerical shearing of the data. If purely absorptive line shapes are desired, processing continues after this stage by the phasing of the $t_2 = 0$ slice, a copying of such phase correction through all t_2 values, and a Fourier transformation of the data as a function of t_2 to yield the final 2D spectrum (Figure 6D).[30] Although not implemented for this data set, weighting and zero-filling can also be applied along the k-axis in a procedure that includes ancillary transformations of the data to and from their conjugate z-domain. As a result of all of this processing, one obtains two sets of 2D $(k/\nu_1,\nu_2)$ data, essentially two NMR spectra, which are mirror-imaged to one another as a result of the opposing gradients employed in the

(29) The most common among these nonidealities arises from the gradients' inability to instantaneously switch between positive and negative values. A certain dead time should thus be added to T_a when computing SW_2, and to T_p when estimating SW_1.

(30) Strictly speaking, points along each k-row do not share identical t_2 evolution values. Such an artifact could be compensated by a minor shearing correction, but this is in fact too small to noticeably influence the spectrum.

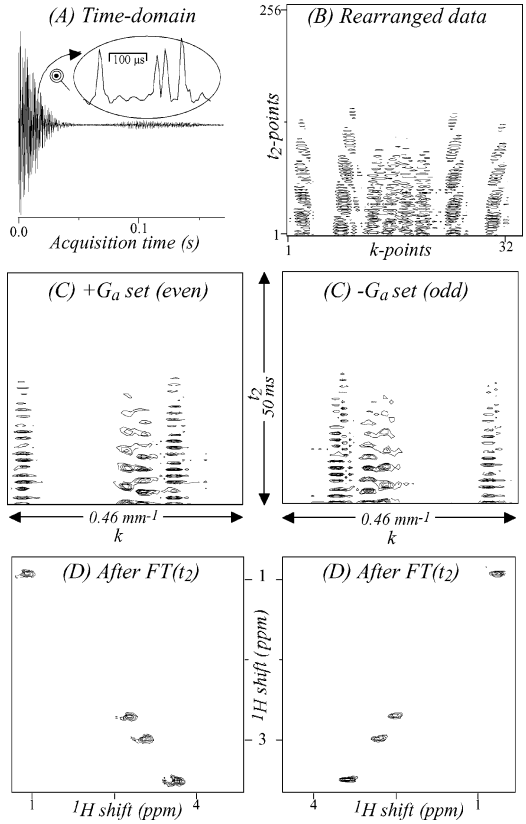

Figure 6. Summary of events involved in the single-scan acquisition of phase-sensitive 2D NMR spectra, illustrated with ^{1}H data recorded on a solution of *n*-butyl chloride dissolved in $CDCl_3$ and utilizing a 2D NMR sequence devoid from the actual mixing process. (A) Time-domain data collected using the spatially selective excitation/detection procedures illustrated in Figures 3 and 4; the magnified inset shows the signal (magnitude) arising from an individual T_a period, depicting in essence the compound's unidimensional ν_1 spectrum. (B) 2D contour plot of the unidimensional data set illustrated in (A), following a rearrangement of its $2N_kN_2$ points according to their k and t_2 coordinates. Interleaved data sets acquired with $+G_a$ and $-G_a$ gradients are still present at this point, thus resulting in a mirror-imaging of the signal along the k-axis. (C) Pairs of data sets resulting upon separating the interleaved $+G_a/-G_a$ arrays in (B) into two (k,t_2) signals possessing N_kN_2 points each. The signals shown in these sets have been subject to a phase correction and to a minor shearing that compensates for nonidealities in the acquisition gradient strengths (see below). Notice the spectral structure observed already at this point along the k-axis. (D) Mirror-imaged 2D NMR spectra arising upon subjecting the data sets in (C) to t_2 Fourier transformation.

scanning of their k-axes. It is thus possible to improve the overall S/N by reversing one of these sets and then combining them both into a single 2D NMR spectrum. As the $+G_a$ and $-G_a$ gradients defining these data sets are rarely of identical magnitudes, care should be exercised in this procedure, and the coincidence of peaks in the two sets should be ensured prior to their recombination.

The 2D NMR data in Figure 6 arise from a sequence deprived of a real mixing process, and hence its peaks are arranged solely along the main homonuclear diagonal. Figure 7 in contrast compares conventional and ultrafast 2D NMR spectra for the model compound when subject to two "real" 2D NMR sequences: COSY, which correlates cross-peaks among directly coupled neighbors, and TOCSY, which establishes cross-peaks among the full system of mutually coupled spins.[5−7] As can be appreciated from this figure, both normal and fast acquisition schemes convey identical spectral information, even if the

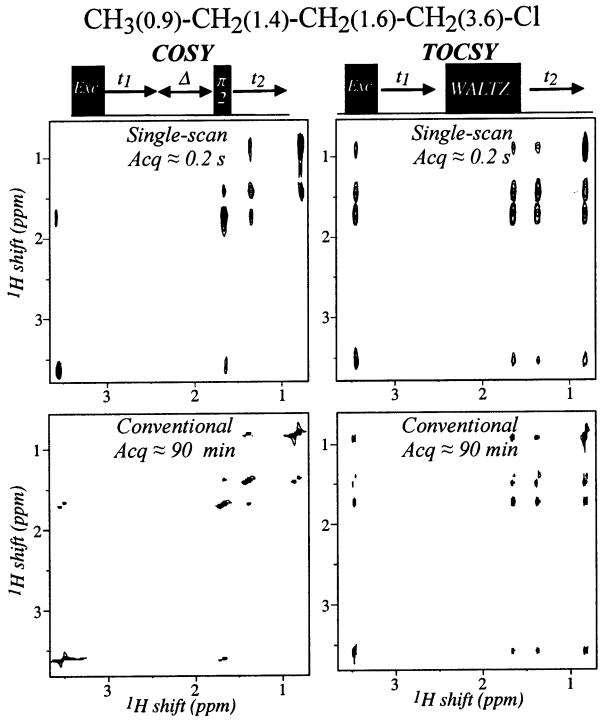

Figure 7. Comparison between conventional and single-scan 2D phased data sets acquired on an *n*-butyl chloride/$CDCl_3$ sample, with the sites' shifts (in ppm) mentioned on top for ease of analysis. As for all of the experiments presented in Figures 6−12, these data were acquired on a Bruker DMX500 NMR spectrometer using a Nalorac TXI probehead. Mixing periods of 20 ms (COSY) and 74 ms (TOCSY) were utilized for the left- and right-hand side panels, respectively. For the single-scan experiments, $N_1 = 40$ initial Gaussian pulses were applied at 4 kHz offset increments while in the presence of $\gamma_e G_e = 150$ kHz/cm, while the acquisition involved $N_2 = 256$ gradient echoes with $T_a = 340$ μs and 10 μs dwell times. All remaining pulses were applied nonselectively. Conventional 2D NMR spectra involving the collection of 128 × 2048 (t_1,t_2) points are also shown for comparison. These latter experiments involved a TPPI phase cycle with 16 scans/t_1 point and 8 dummy scans.

resolution in ultrafast experiments is lower if a limited number of N_1 slices (akin to the t_1 points in a conventional acquisition) are used in their collection. Factors influencing spectral resolution and routes to improve it by what can in principle be an arbitrary extent are further discussed below.

The examples in Figures 1, 6, and 7 involve correlations where chemical shift ranges are relatively small. The spectral width of the indirect domain can therefore be scanned using weak gradients, and minor gradient switching dead times adding to T_p and T_a (and, therefore, detracting from the achievable SW_1 and SW_2 ranges) are acceptable. Different, however, is the situation in Figure 8, dealing with a peptide requiring spectral width ranges in the order of 9 ppm. Gradients that are fast as well as intense can still deliver in these situations the desired spectral range, yet at the expense of exceeding most performance characteristics for currently available spectroscopic probeheads.[31] The stringency of these gradient requirements can be lifted if data are collected over a few, rather than within a single, scans. Figure 8 illustrates this alternative, with the acquisition of 2D TOCSY ^{1}H NMR spectra on a model hexapeptide using one, two, and three scans, respectively. Shown as well for the sake

(31) In terms of intensities and duty cycles, superior gradient specifications are usually met by microimaging NMR systems. These were actually assayed during the course of our studies, yet generally found lacking in terms of their sensitivity and gradient-recovery characteristics.

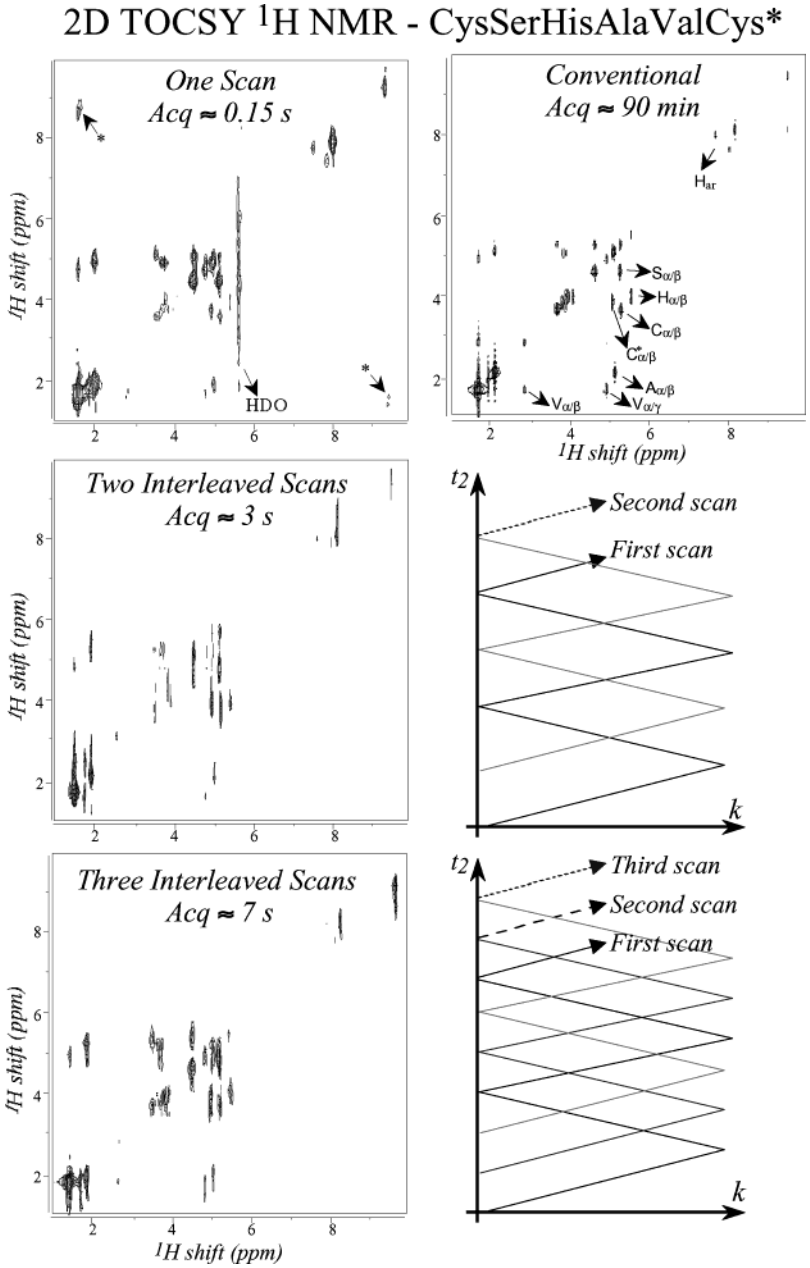

Figure 8. Acquisition strategies capable of easing the gradient demands of ultrafast NMR, based on extending the single-transient 2D experiment to a small number of interleaved scans spanning the *k*-space trajectories illustrated to the right of each spectrum. 2D TOCSY spectroscopy (50 ms WALTZ mixing, magnitude plotting) was chosen to illustrate these acquisition modes, using a solution of the indicated hexapeptide dissolved in D_2O (whose residual water resonance was largely eliminated using a 1.5 s presaturation pulse). Acquisition parameters for the various ultrafast experiments included $N_1 = 61$, $N_k = 66$, $N_2 = 256$, $\Delta O = 12$ kHz, $\gamma_e G_e = 300$ kHz/cm, $\gamma_a G_a = 300$ kHz/cm, 1 μs dwell times, and 80 μs Gaussian excitation pulses for the single-scan acquisition; $N_1 = 23$, $N_k = 23$, $N_2 = 256$, $\Delta O = 8$ kHz, $\gamma_e G_e = 110$ kHz/cm, $\gamma_a G_a = 97$ kHz/cm, 8 μs dwell times, and 100 μs Gaussian excitation pulses for the two-scan acquisition; $N_1 = 35$, $N_k = 35$, $N_2 = 256$, $\Delta O = 8$ kHz, $\gamma_e G_e = 180$ kHz/cm, $\gamma_a G_a = 90$ kHz/cm, 8 μs dwell times, and 100 μs Gaussian excitation pulses for the three-scan acquisition. Most remaining experimental conditions were as in Figure 7. The differing ν_1 resolution observed among the various spectra is a consequence of the different number of N_1 slices chosen to carry out the acquisitions, and not of the increasing number of scans that were used. Asterisks in the single-scan acquisition indicate peaks arising from the "ghosting" phenomena further described in the text. A conventional 2D NMR spectrum showing a tentative assignment of the resonances is also illustrated for completion on the top-right panel.

of comparison is the normal 2D spectrum of the peptide collected over 128 t_1 increments. Illustrated to the side of each multiscan plot is the manner by which data arising from these *N*-scan experiments were interleaved to reconstruct the 2D (k,t_2) data sets which were eventually transformed. This data interleaving is based on inserting additional $\{i/(NT_a)\}_{i=0,N-1}$ free evolution delays prior to the application of the $+G_a/-G_a$ gradient trains. This enables the use of longer T_a values (and/or the inclusion of moderate gradient dead times), while still yielding acceptable $SW_2 = N/2T_a$ spectral windows. As opposed to alternative EPSI-type schemes that avoid the use of such free evolution delays by manipulating the timing of $\pm G_a$ gradient trains, we find that—at least within our limited range of preliminary tests—the interleaved data procedure exemplified in Figure 8 yields cleaner final spectra and fewer artifacts.

The spatial-encoding principles that were illustrated so far for monitoring 2D homonuclear connectivities can also be employed for implementing heteronuclear correlations. Such

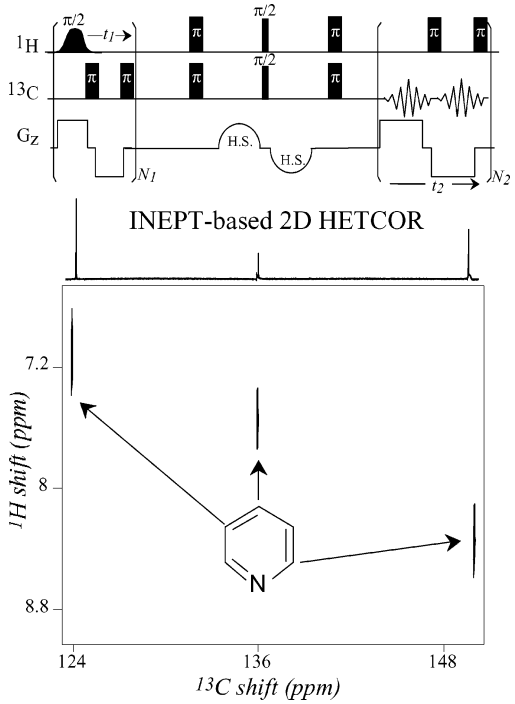

Figure 9. 2D ^{1}H−^{13}C single-scan NMR spectrum obtained on pyridine/$CDCl_3$ using the directly detected heteronuclear correlation sequence sketched on top, which involves a spatial-encoding of the ^{1}H magnetization and subsequent decoding on the ^{13}C channel. Data acquisition parameters included $N_1 = 33$, $N_k = 29$, $N_2 = 360$, $\Delta O = 4$ kHz, $\gamma_e G_e = 38$ kHz/cm, $\gamma_a G_a = 50$ kHz/cm, 256 μs Gaussian excitation rf pulses, 5 μs dwell times, and homospoil (H.S.) gradients tuned to select the $H_xC_z \rightarrow H_zC_x$ coherence transfer. The total acquisition time was in this case ∼200 ms; other details are as in Figure 7.

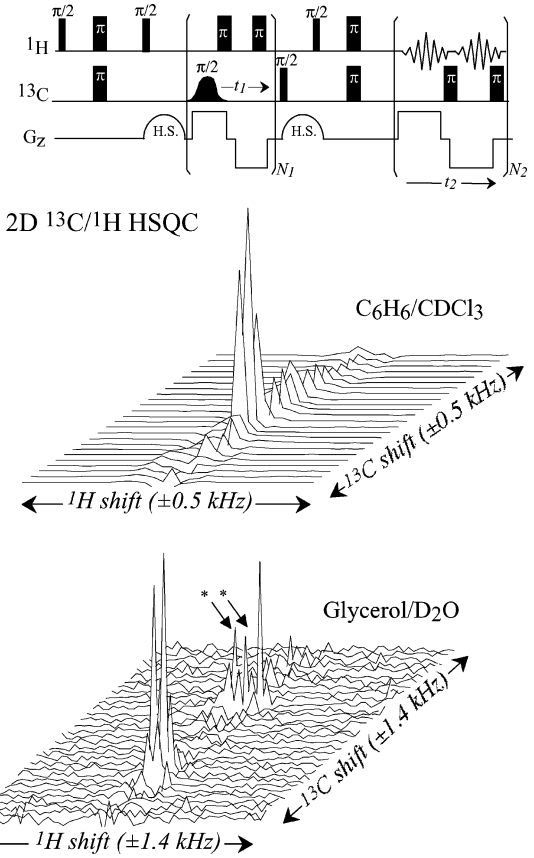

Figure 10. 2D ^{1}H−^{13}C phase-sensitive NMR spectra obtained on the indicated samples at natural abundance, using the HSQC-type sequence sketched on top. Data acquisition details included $N_1 = 20$, $N_k = 32$, $N_2 = 128$, $\Delta O = 4$ kHz, $\gamma_e G_e = 40$ kHz/cm, $\gamma_a G_a = 97$ kHz/cm, and other parameters as in Figure 9. Two scans with the selective ^{13}C pulse (and the receiver) phase-cycled by 180° were collected for the sake of removing residual ^{1}H−^{12}C background signals; asterisks in the glycerol spectra correspond to "ghosts" arising along the indirect dimension from the methylene peaks.

experiments will rely on applying the Ω_1-driven spatial winding of magnetizations on a particular spin species *S*, preserving this encoding as an amplitude modulation during a mixing which implements a heteronuclear $S \rightarrow I$ transfer, and then decoding this information during the acquisition by gradients applied on the second *I* species. Figures 9 and 10 illustrate how two sequences that form the basis of several directly and indirectly detected heteronuclear correlation experiments[9,10,12] can be modified for their single-scan execution. The first of these sequences is based on a ^{1}H t_1 evolution followed by an INEPT-based transfer period; the fact that t_1 in this sequence is triggered by a simple 90° excitation enables the introduction of a spatial-encoding in ways that are entirely parallel to the ones implemented in the homonuclear correlations (Figure 9, top). The only major distinction with the conventional 2D sequence then arises from the inability of conventional decoupling sequences to achieve their aim while under the action of intense oscillating gradients. Such goals were consequently implemented during both the ^{1}H and the ^{13}C free evolution periods, by inserting 180° pulses within the complementary rf channel during the course of the $+G/-G$ transition delays. The same decoupling principle was incorporated in the second of the heteronuclear correlation sequences assayed, HSQC (Figure 10). In contrast to its directly detected counterpart, this sequence begins with a multipulse refocused INEPT block that is not susceptible to a simple spatial-encoding. Still, a spatial winding of magnetizations could be incorporated by shaping the 90° pulse that triggers the $H_zC_z \rightarrow H_zC_x$ conversion, and with it the t_1 evolution, following the first INEPT block. Phase cycling this selective excitation together with the receiver by 180° also helped to clean these acquisitions from otherwise residual natural-abundance ^{1}H−^{12}C signals. Such a two-scan phase cycling procedure was not found necessary when dealing with properly tuned experiments on isotopically enriched samples (data not shown).

In addition to a stepwise t_1 incrementation, a common NMR approach to encode indirect evolution frequencies relies on systematically varying the location of a 180° pulse through the duration of a constant evolution period τ.[6,7] Such a pulse will refocus the linear evolution terms (chemical shifts and heteronuclear couplings), yet leave homonuclear couplings unaffected, thus providing an appealing option to achieve homonuclear decoupling. The spatial-encoding scheme introduced in this study can also be incorporated into this so-called constant-time modality, as illustrated by the example shown in Figure 11. This ultrafast scheme achieves a spatial-encoding not by incrementing the initial excitation pulse but by using a single 90° excitation, which is subsequently followed by a train of spatially selective 180° refocusing pulses. An $\exp[i\Omega_1(\tau - 2Cz)]$ shift-driven winding of magnetizations is then imposed on the sample, from which the ν_1 frequency spectrum can be decoded via the *k*-space protocol just as described before. As illustrated by the butyric anhydride example shown in Figure 11, purely absorptive line shapes are again a possibility in this kind of acquisition mode;

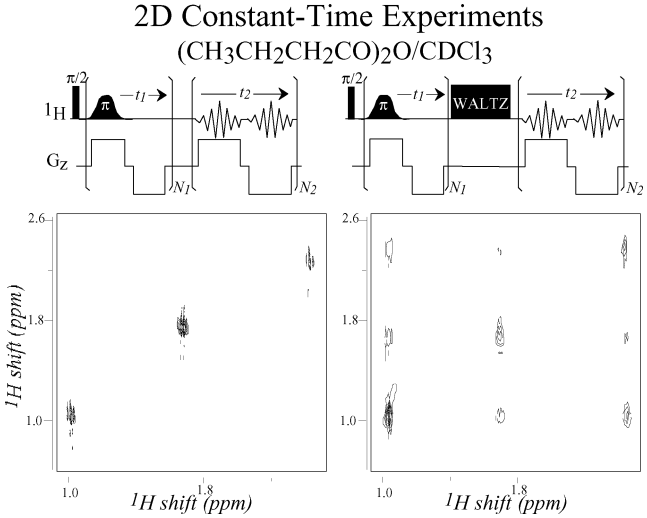

Figure 11. 2D phase-sensitive single-scan ^{1}H NMR spectra collected on a $CDCl_3$ solution of butyric anhydride, using the constant-time modality sequences schematized on top of each contour. Data acquisition details included $N_1 = 26$, $N_k = 65$, $N_2 = 160$, $\Delta O = 4$ kHz, $\gamma_e G_e = 77$ kHz/cm, $\gamma_a G_a = 46$ kHz/cm, dwell time = 8 μs, 400 μs Gaussian 180° pulses. A 50 ms long WALTZ mixing was used in the TOCSY acquisition (right).

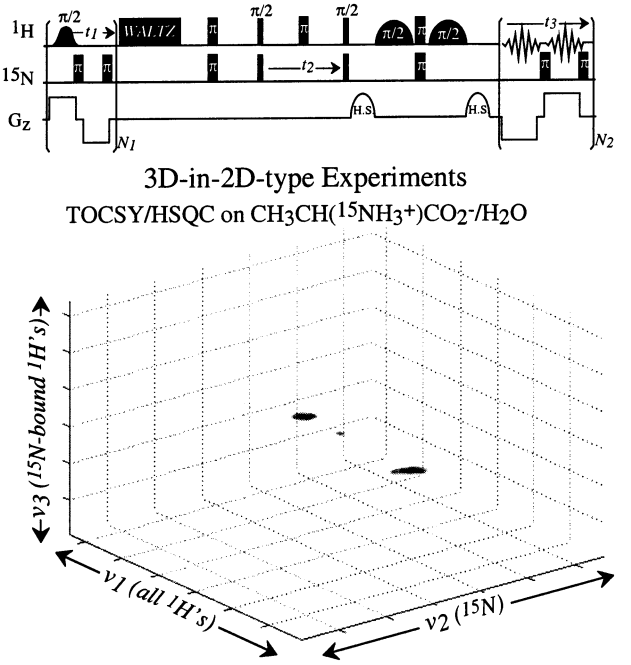

Figure 12. 3D phase-sensitive ^{1}H−^{15}N−^{1}H TOCSY/HSQC NMR spectrum collected on ^{15}N-labeled alanine dissolved in a pH = 1 93%/7% H_2O/D_2O solution, using the sequence schematized on top. Spatial-encoding was employed to monitor the initial set of evolution frequencies within a single scan, while a conventional hypercomplex incrementation (32 values for independent cosine/sine sets) was carried out to encode the ^{15}N evolution frequencies during the course of t_2. Other acquisition details included $N_1 = 26$, $N_k = 64$, $N_2 = 128$, spectral widths SW_{1-3} equal to 8.5, 10, and 3 ppm, respectively, 90 ms TOCSY mixing time, 4 s recycle delay, and a WATERGATE-based suppression of the water signal prior to data acquisition.[32]

further peculiarities of constant-time as opposed to normal ultrafast 2D NMR experiments will be described elsewhere.

We conclude this experimental section by discussing the possibility of combining the new ultrafast methodology with traditional 2D NMR schemes, to accelerate the acquisition of higher-dimensional NMR spectra. Figure 12 illustrates how 3D NMR spectra can be collected over extents of time that would normally be associated to 2D NMR acquisitions, using a TOCSY−HSQC NMR sequence as an example.[10] Such an experiment begins with an initial spatial-encoding applied on the ^{1}H system; coherences thus excited are then allowed to transfer among the homonuclear network via an isotropic mixing and ported into ^{15}N coherences via an INEPT block. These ^{15}N coherences are thus generated with a spatial-encoding and subsequently allowed to evolve in a normal fashion over an intermediate evolution time t_2. The two-spin H_zN_x coherences are finally transformed into transverse single-quantum ^{1}H magnetizations, on which the spatial decoding is carried out. The coherent nature of all mixing processes then enables the acquisition of a purely absorptive 3D TOCSY−HSQC (^{1}H−^{15}N−^{1}H) NMR spectrum within the time it would take to run a conventional 2D HSQC experiment, roughly 10 min for the aqueous ^{15}N-alanine solution on which it was assayed.

Discussion

Line Shape Considerations. Having considered the basic principles of single-scan 2D NMR and illustrated the method's execution with a number of simple examples, we dwell in this section on a finer discussion of the methodology's features. For the sake of clarity, we shall confine such a description to conventional (nonconstant-time) 2D NMR experiments. We begin by focusing on the basic scenario illustrated in Figure 5, which explores how signals along the *k*-axis are formed during the course of the first gradient echo period, and use it to derive a mathematical expression for the observable peak shapes. To do so, we begin by neglecting relaxation and Ω_2 shift effects and associate to each of the N_1 discrete slices excited by selective pulses during the course of the initial evolution period its own individual magnetization vector. According to the protocol laid out in the Methods section, these spin-packets will end up equally spaced throughout the sample's length L at positions $\{z_j = [L/(N_1 - 1)][j - (N_1 - 1)/2]\}_{j=0,N_1-1}$ and will contribute with identical weights to the overall $S(k)$ signal that is detected. When acted upon by the acquisition gradient G_a, the spin-packets within such discrete slices will be endowed with instantaneous precession frequencies $\nu_j = z_j \gamma_a G_a$. The signal originated as a function of $k = \gamma_a \int_0^t G_a(t')\,dt'$ can then be written as

$$S(k) = \sum_{j=0}^{N_1-1} F_j e^{ikz_j} \qquad (6)$$

The $\{F_j\}_{j=0,N_1-1}$ coefficients here are a complex set describing the state of the spin-packets at the $k = 0$ instant; they are the $x-y$ magnetizations associated to the various spatial slices, to which we ascribe a *j*-dependence which accounts for the Ω_1 frequency that may have been active during the initial t_1 evolution period. Such spin-packets can consequently be written as $F_j = (A/N_1)e^{i\Omega_j t_1(z_j)}$, A being the overall magnetization expected from a particular site when considered over the whole sample. On the basis of Figures 2, 3, one can further express the evolution times t_1 experienced by magnetizations within each of these slices as $t_1(z_j) = C\cdot(z_j - z_{N_1})$, where the $C = \Delta t_1 \gamma_e G_e / \Delta O$ coefficient depends on the spacing between consecutive selective excitations. Assuming as done earlier an ideal dwell time Δt_1 equal to twice the excitation pulse T_p as well as $\gamma_e G_e /$

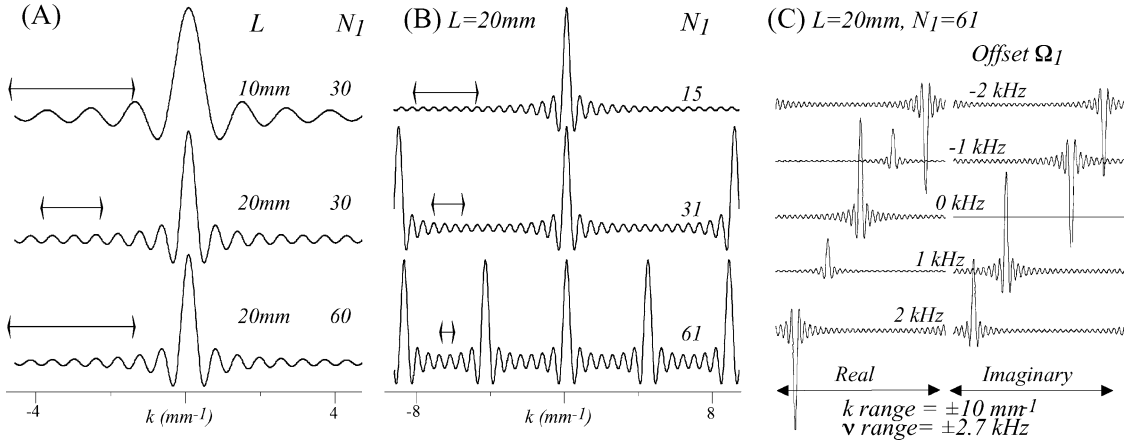

Figure 13. Plots of the $S(k)$ function introduced in eq 11 for a variety of relevant cases. All plots were calculated for a fine Δk increment (1000 values equally distributed over the indicated ranges), and therefore their signals' variations reflect the excitation (N_1, Ω_1, L) rather than the acquisition conditions. (A) Line shapes resulting for $\Omega_1 = 0$ as a function of L and of different N_1 increments (slices). (B) The same as (A) but for a fixed L and over a larger k-range, showing the appearance of "ghost" peaks flanking the main $k = 0$ echo as N_1 increases. (C) Line shape effects introduced by varying Ω_1 frequencies, involving both a displacement and a phase shift of the echoes from their initial $k = 0$ position. Arrowhead markers in panels A and B correspond to the equivalent length spanned by a 1 kHz frequency range along the indirect dimension axis.

$\Delta O > 0$ leads to $C = 2T_p(1 - N_1)/L$. Using all of these definitions for z_j, F_j, t_1, and C, we rewrite eq 6 as

$$S(k) = \frac{A \cdot e^{iT_p(N_1+1)\Omega_1}}{N_1} \cdot e^{i\epsilon/2} \cdot \sum_{j=0}^{N_1-1} [e^{-i\epsilon/(N_1-1)}]^j \qquad (7)$$

where $\epsilon = 2\Omega_1 T_p(N_1 - 1) + kL$. The geometric series in eq 7 can be evaluated using the well-known relation $\sum_{j=0}^{N-1} z^j = (1 - z^N)/(1 - z)$, leading to

$$S(k) = \frac{A \cdot e^{iT_p(N_1+1)\Omega_1} e^{i\epsilon/2}}{N_1} \cdot \frac{1 - e^{-i\epsilon N_1/(N_1-1)}}{1 - e^{-i\epsilon/(N_1-1)}} \qquad (8)$$

which can also be rewritten as

$$S(k) = \frac{A \cdot e^{iT_p(N_1+1)\Omega_1}}{N_1} \cdot \frac{e^{i\epsilon/2} e^{-i(1/2)\epsilon N1/(N_1-1)}}{e^{-i(1/2)\epsilon/(N_1-1)}} \cdot \frac{e^{i(1/2)\epsilon N_1/(N_1-1)} - e^{-i(1/2)\epsilon N_1/(N_1-1)}}{e^{i(1/2)\epsilon/(N_1-1)} - e^{-i(1/2)\epsilon/(N_1-1)}} \qquad (9)$$

As the ratio in the middle of this expression is unity, eq 9 yields

$$S(k) = \frac{A \cdot e^{iT_p(N_1+1)\Omega_1}}{N_1} \cdot \frac{\sin\left[\frac{1}{2}\epsilon N_1/(N_1 - 1)\right]}{\sin\left[\frac{1}{2}\epsilon/(N_1 - 1)\right]} \qquad (10)$$

On considering $N_1 \gg 1$, we have $N_1 + 1 \approx N_1$, $N_1/(N_1 - 1) \approx 1$, and $1/(N_1 - 1) \approx 1/N_1$; using these approximations and replacing back for ϵ's expression results in the relatively simple line shape expression

$$S(k) = \frac{Ae^{iT_p N_1 \Omega_1}}{N_1} \cdot \frac{\sin\left(\Omega_1 T_p N_1 + \frac{kL}{2}\right)}{\sin\left(\Omega_1 T_p + \frac{kL}{2N_1}\right)} \qquad (11)$$

It is convenient to consider the implications arising from eq 11 on assuming $\Omega_1 = 0$, as $S(k)$ describes then the point-spread function characterizing the peaks' shapes along the indirect domain of these experiments. Figure 13A plots out the line shapes that in this shift- and relaxation-free scenario are observed for a variety of cases. As expected, the resulting function is always defined and real and exhibits at $k = 0$ a maximum value A regardless of the number of slices or of the sample's length. This is reflecting the fact that the k-axis echoes making up the indirect-domain signals in this kind of experiment arise from the constructive interference of spin-packets throughout all of the sample. Hence, aside from losses incurred due to the mixing process or to pulse imperfections, the overall magnitudes expected for peaks in this type of acquisitions will be comparable to those arising from a single-scan NMR experiment.[33] It is worth remarking, however, that the situation will be different with regards to the noise level. When setting up conventional 2D NMR experiments under the conditions derived above for the single-scan acquisition, where dwell times along the directly detected domain are given by $2T_a$, the filter of the spectrometer would be accommodated to accept a noise bandwidth in the order of $(2T_a)^{-1}$. In contrast and as mentioned above (Figure 4), the ultrafast acquisitions need much shorter dwell times—ca. $2N_k$ times smaller—to allow for the simultaneous sampling of data along both frequency axes. Filter bandwidths will thus need to be opened by a similar factor, leading to $\sqrt{2N_k}$ larger levels of incoming noise. Given the demand to collect a complete multidimensional spectrum in a single scan, it is hard to envision how such a penalty could eventually be avoided. Systematic noises arising from gradient nonidealities and further treated below are also expected to affect the effective S/N observed in this kind of experiment.

Equation 11 also predicts that, at least under ideal relaxation-free conditions, purely absorptive line shapes will be built-in features of the ultrafast 2D NMR experiment. Indeed, on considering $\Omega_1 = 0$ and the usual $N_1 \gg 1$ situation where $\sin(kL/2N_1) \approx kL/2N_1$, $S(k)$ can be approximated in the $k \approx 0$ neighborhood as $\mathrm{sinc}(kL/2)$. Incorporating then the FT of the

(32) Piotto, M.; Saudek, V.; Sklenar, V. *J. Biomol. NMR* **1992**, *2*, 661.
(33) Gradient echoes are usually associated with signal losses arising from random molecular diffusion, which could also influence this experiment. Yet an estimation of these effects based on Stejskal and Tanner's equation, $S_{i+1}/S_i = \exp[-(\gamma G)^2 \cdot \delta^2 \cdot D \cdot (\Delta - \delta/3)]$,[34] predicts a per cycle attenuation on the order of $\exp[-(10^5)^2 \cdot (10^{-4})^2 \cdot 10^{-5} \cdot 10^{-4}] \approx 0.9999$. Even considering hundreds of $N_1 + N_2$ cycles, we found that these diffusion losses will be negligible; with the addition of $\Delta \approx 0.1$ s mixing periods, such losses may begin to be noticeable, even though they still will not be significant.

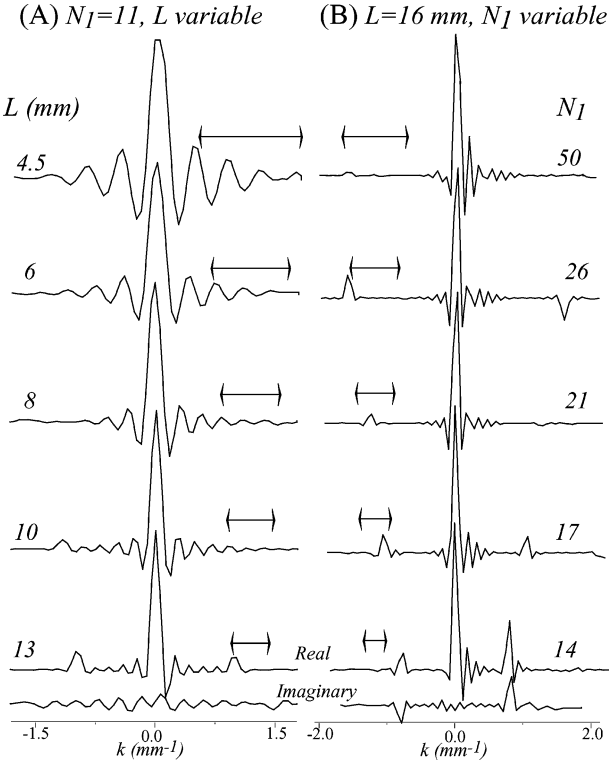

Figure 14. Experimental corroboration of the $S(k)$ expectations illustrated in Figure 13A,B, as manifested by the single-site real signal arising from on-resonance HDO. In all cases, a mixing-less experiment was carried out (Figure 6), and the signal observation was confined to the first gradient echo along the direct acquisition domain. The bottom trace also illustrates the imaginary residual obtained upon properly phasing the corresponding k-signal; similarly negligible residuals were observed in the imaginary channels of all traces. In addition to the indicated parameters, the acquisitions involved $N_k = 256$, $\gamma_e G_e = \gamma_a G_a = 117$ kHz/cm, 256 μs Gaussian excitation pulses. As in Figure 13, markers indicate here a 1 kHz frequency span.

conventional $\exp(i\Omega_2 t_2)\exp(-t_2/T_2)$ modulation defining the spin's evolution along the directly detected axis leads to $I(k/\nu_1,\nu_2)$ 2D NMR line shapes whose real components can be cast after suitable phasing as $\mathrm{sinc}(\nu_1)$ $\mathrm{Lorentzian}(\nu_2)$. Such a kernel possesses convenient site-resolving characteristics. The full-width at half-height resulting then for peaks along the k/ν_1-axis will be given by fwhh $\approx 7.6/L$, an apparent line width that in k-units (although not on a frequency scale, see below) becomes solely defined by the sample's length. On considering the line shape effects introduced by increasing the number of slices, it turns out that N_1 is influential mainly in decreasing the intensities of the "wiggles" flanking the $k \approx 0$ peak. All of these expectations are fully born out by experiments (Figure 14A).

In contrast to a conventional sinc function, the $S(k)$ signal resulting from eq 11 for the $\Omega_1 = 0$ case will peak into a maximum not only for $k = 0$, but also whenever $kL/2N_1$ becomes an integer multiple of π. This condition will make both the numerator and the denominator in eq 11 null, leading to the appearance of sinclike "ghosts" flanking the peak at the origin (Figure 13B). This prediction, which is again fully reflected by experiments (Figure 14B), constitutes perhaps the most common type of artifact affecting this kind of 2D NMR spectroscopy. Equations aside, the generation of these ghosts can again be understood from the basic cartoon in Figure 5, which depicts k-echoes as arising in these experiments from the constructive interference between magnetizations precessing at multiples of a basic frequency $\Delta O \cdot \gamma_a G_a/\gamma_e G_e$. The fact that the frequencies of these magnetizations are all equally spaced implies that spin-packets will meet repetitively at time intervals given by the inverse of the basic frequency, with the occurrence of this "ghosting" becoming more common as the basic frequency ΔO increases (or equivalently for fixed L and $\gamma_e G_e$ values, decreasing N_1—Figure 14B). When translated into k-units, this frequency-based argument agrees with eq 11, in predicting that "ghost" peaks will appear at multiples of $\Delta k = |\gamma_e G_e/\Delta O| = N_1/L$. In most homonuclear instances that we have encountered, such ghosts can be placed outside the region of spectral interest. Yet unless improvements are made on currently available spectroscopic-gradient technologies, the relatively low γ_e/γ_a ratios involved will prevent this from being the typical case for heteronuclear correlations. Still, good use can be made even in these instances of this effect via the deliberate "folding" of ghost peaks within the acquisition window. Examples of these phenomena, together with strategies for deleting these ghosts by combining signals acquired in independent experiments, will be discussed elsewhere.

Two main changes affect these basic line shapes upon considering the introduction of chemical shift effects. First, of course, is a shifting of the echo maxima from their $k = 0$ condition (Figure 13C). Inspection of eq 11 predicts that echo peaks $S(k)$ will then map the Ω_1 frequencies according to

$$\Omega_1 = -\frac{L}{2N_1 T_p} k + \frac{m\pi}{T_p}, \quad m = 0, 1, \ldots \tag{12}$$

The first term on the right-hand side of eq 12 can also be written as $[\Delta O \gamma_a \int_0^{t_2} G_a(t)\,dt]/\gamma_e G_e \Delta t_1$, and is the one responsible for unraveling the shifts that occurred during t_1 in terms of echo positions along the k-axis. The second term is responsible for a "ghosting" process similar to that mentioned for $\Omega_1 = 0$, which will repeat peaks (in frequency units) by multiples of T_p^{-1}. As for the line shapes that k-peaks will possess, these will be as for the $\Omega_1 = 0$ case (i.e., sinclike) yet no longer purely real. Indeed, the fact that the $t_1 = 0$ condition does not correspond with the $z = 0$ slice imposes a large $e^{i(N+1)T_p\Omega_1}$ first-order phase distortion although as demonstrated in the preceding section, purely absorptive peaks can in principle be obtained by an appropriate phase correction of the signals. The width of these peaks can be approximated (in frequency units) as fwhh $\approx 3.8/(N_1 T_p)$, implying that a sufficiently large number of N_1 slices can achieve what is in principle an arbitrary degree of spectral resolution; this, of course, provided that sufficiently intense excitation gradients are available.

So far, we have circumscribed to the scenario depicted in Figure 5 to derive basic line shape characteristics for single-scan 2D NMR spectroscopy. Still, by considering the signals arising from each of the excited slices as being associated to magnetizations' vectors possessing constant amplitudes, this picture simplifies an important feature pertaining to the ongoing events: the dephasing/rephasing processes that magnetizations within individual slices will undergo when acted upon by gradients. As a result of these processes, the A amplitude involved in eq 11 will become itself a function of k. It can actually be shown (Appendix) that, when utilizing nonoverlapping selective pulses and while in the validity region of the linear excitation approximation, this $A(k)$ function will reflect the shape $E(t)$ of the rf pulses that are used to achieve the

selective excitation of the individual slices. In other words, reliance on excitation pulse shapes given by amplitude-dependent envelopes $E(t)$ will lead to an additional "weighting" of the $S(k)$ signals given in eq 11, which can be accounted for by replacing the constant A by a k-dependent enveloping function

$$A(k) = E\left(\frac{T_p}{2} - \frac{k}{\gamma_e G_e}\right) \tag{13}$$

Using Gaussian excitation pulses will thus weight the apparent amplitudes of peaks along the k-axis by a Gaussian centered at $\gamma_e G_e T_p/2$, sinc pulses will weight the spectrum by $\gamma_e G_e T_p/2$-centered sinc functions, etc. This phenomenon has a number of important consequences toward defining the appearance of the spectra. First, it follows from these arguments that under common homonuclear operational conditions ($T_p \approx T_a/2$, $G_e \approx G_a$) the amplitude of peaks in the $k \approx 0$ neighborhood will be very small, almost negligible. To correct for this feature, which could deprive the technique from much of its usefulness, we carry out the ultrafast 2D NMR experiments utilizing a time-proportional phase incrementation (TPPI) of the selective pulses. This procedure adds an artificial extra winding to the spin-packets associated to the individual slices which, independent of either gradient or shift-evolution, will displace the location of the echo peaks by an arbitrary amount along the k-axis. For instance, given $\Delta O = 1/T_p$ and a shifting of consecutive pulses by 180°, spectra collected under the above-mentioned conditions will become centered around the $k_o = \gamma_e G_e T_p/2$ point of maximum intensity.[35] A second consequence of this k-dependence in the magnetizations' amplitudes is that, in contrast to what is predicted by eq 11, peak amplitudes in ultrafast 2D NMR will not reach their full, ideal intensities A; they will be weighted by the pulses' shape. Finally, the ghost peaks predicted by eq 12 will not extend through arbitrarily large ranges of m-values: their amplitudes will rapidly decay, as ghosts become displaced from the center of the envelope that is defined by eq 13. Thus, even under conditions that are conducent to the appearance of ghost artifacts, it is rare to observe more than one or two such peaks arising from a particular chemical site (Figure 15). Also worth noting is the slice-independence and purely real character of the $A(k)$ weighting functions, a feature which frees this effect from changing the position or shape of peaks throughout the ν_1- or ν_2-domains.

Consequences of Gradient Nonidealities. Before concluding this Discussion, it is worth addressing certain aspects pertaining to the relevance of the gradients' quality. Gradients are, of course, of essence to this methodology. Intense gradients applied over extended sample lengths could afford what is in principle an arbitrary spectral resolution along the ν_1-axis, and the maximization of these parameters should be sought. Also addressed earlier were issues of gradient switching and settling times, which largely define the compromise that in single-scan acquisitions can be achieved between the SW_1 and SW_2 maximum spectral widths. Two other issues that we find worth exploring relate to the accuracy and the constancy demanded from the gradient amplitudes throughout the various stages of the experiment. These issues were investigated with the aid of an appropriate numerical simulation program, as nonidealities can be better followed in such fashion. Particular attention was placed on computing the effects that two common artifacts, gradient drooping and an imbalance between $+G/-G$ gradient intensities, would have on the 2D spectral line shapes. Expectations from these calculations are illustrated in Figure 16A and B, respectively. We observe that, while deviations from ideality remain small, the main consequence of an overall drop in the gradient's strength is a "tilting" of the k-axis echoes as t_2 progresses. This tilting reflects the increasing delay required by weakened gradients toward the formation of k-axis echoes and constitutes a feature that as already mentioned was repeatedly observed throughout the course of our experiments. As long as this drooping effect is linear with t_2, it can be compensated numerically by a shearing of the data prior to its FT, even if a slight resolution penalty is still paid in terms of the k-axis line shapes. In some cases—encountered, for instance, with the gradients of cryogenic probeheads—we observed nonlinear droops that could not be corrected in such simple fashion. Resolutionwise, a heavy price is then paid in terms of the line shapes characterizing the peaks. Severe line shape distortions also arise when dealing with a systematic imbalance between $+G$ and $-G$ gradients (Figure 16B). This results in broadened peaks along the ν_1-axis, whose numerical compensation via a software correction appears unlikely. In the case of the experiments discussed throughout this work, severe distortions of these nature were not observed, and no efforts were thus made to compensate for them.

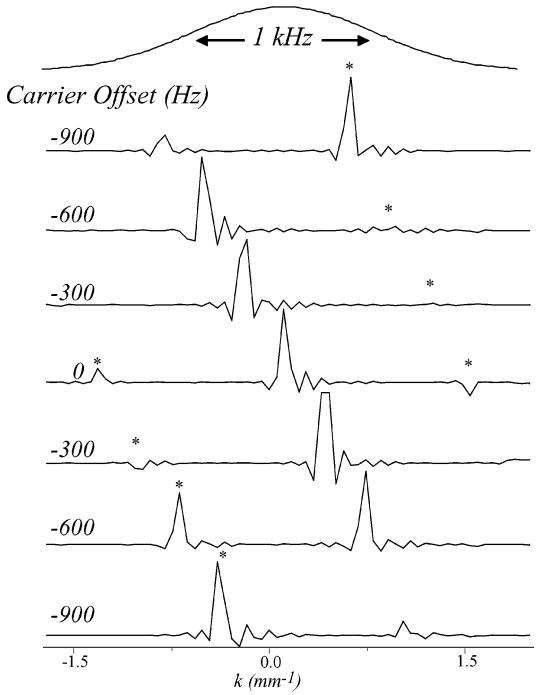

Figure 15. The same as in Figure 14, but this time illustrating the appearance and nature of "ghost" peaks (marked by asterisks) during the course of the refocusing acquisition gradients. Experiments involved fixed N_1, L, and ΔO values (26, 16 mm, and 8 kHz respectively); they were repeated as a function of the basic carrier offset, and subsequently phased to yield null center-peak imaginary components. The curve on top of the traces illustrates the expected $A(k)$ envelope (eq 13), which weights the various echoes predicted in Figure 13B according to their position along the k-axis.

(34) Stejskal, E. O.; Tanner, J. E. *J. Chem. Phys.* **1965**, *42*, 288.
(35) Alternatively, under certain appropriate conditions (e.g., $\Delta O \approx 2/T_p$, $T_a = 2T_p$), it is possible to forego the TPPI procedure altogether and obtain ghost-based spectra where all peaks are shifted along the k-axis by the $m = \pm 1$ condition (eq 12). Because of the periodicity of the ghosting process, which affects all peaks in an identical fashion, such spectra are indistinguishable from those arising for $m = 0$ and the use of TPPI.

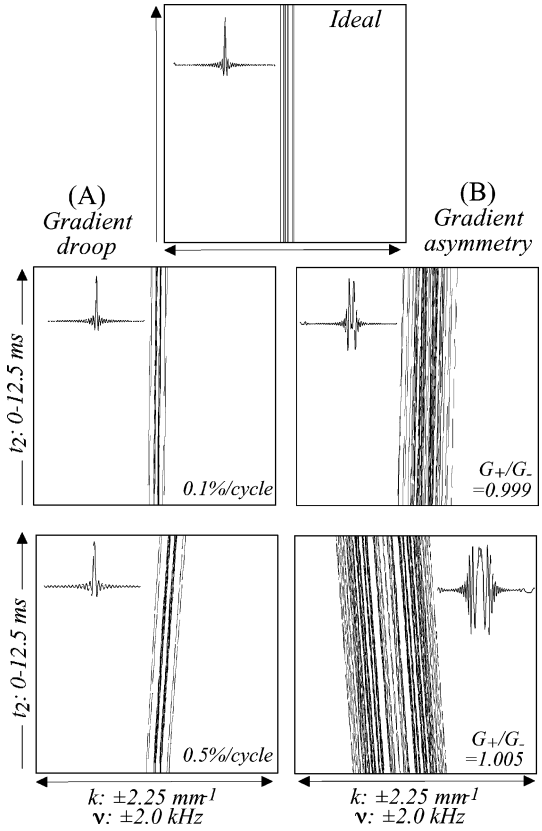

Figure 16. Variations expected on $S(k,t_2)$ data collected during single-scan 2D experiments, as a result of two common gradient-related nonidealities. (A) Distortions arising from a drop in the gradient's strength as a function of the excitation/acquisition $\pm G$ cycles. (B) The same as (A) but for gradients possessing a strength imbalance between their positive and negative values. For ease of visualization, only one of the two sets resulting from the EPSI processing of raw data was illustrated (the one corresponding to $+G_a$), and both an ideal 2D data set as well as cross sections of the peaks expected for each instance along the *k*-axis were also included. All of these simulations assumed $N_1 = 45$, $N_k = 100$, $N_2 = 50$, $\Delta O = 8$ kHz, $\gamma_e G_e = \gamma_a G_a = 180$ kHz/cm, dwell time = 1 μs, and 250 μs long Gaussian 90° pulses. To carry out these calculations, a Matlab 6.2 (The MathWorks Inc.) code was developed, whereby the overall sample was subdivided into a large number of *z* slices (over 300 in the present case), the spin evolution for each of these slices was computed under the effects of all pulses and gradients via the numerical integration of their position- and time-dependent Bloch equations, and the signals arising from the corresponding spin-packets were subsequently co-added into a final sample FID. Using a 1 μs time-propagation interval, we found that such 2D NMR data computations required ca. 5′ to execute on a 2.4 GHz Pentium IV PC.

Conclusions and Perspectives

It is clear that valuable opportunities could be opened up by reducing the acquisition times required to collect multidimensional NMR spectra. Such opportunities have been realized during the past decade in the field of MRI with the introduction of echo-planar and low-angle excitation methodologies, techniques which, although highly efficient when dealing with gradient-based interactions, do not find a straightforward extension within a purely spectroscopic setting. Methods to accelerate the acquisition of multidimensional NMR spectra have therefore relied, for the most part, on more efficient data processing approaches, on cleverly tailored excitation schemes, or on both.[36−39] In contrast, the methodology that we have discussed in this work speeds up the acquisition of full 2D NMR data sets by relying on the use of magnetic field gradients. In combination with the consecutive excitation of individual slices within the sample, this leads to what appears to be a general way of parallelizing what has hitherto been the serial acquisition of independent t_1-encoded signals. The main purpose of the present account was to introduce a description of the resulting methodology which, although still involving mathematical and numerical details, gives physical insight a priority. The starting point of this description thus focused on conveying the potential that is opened up by the spatial-encoding of the internal spin evolution frequencies, an idea which lies at the core of our parallelization of 2D NMR. Using simple FT concepts, we could then show how gradient echo schemes are able to retrieve in a rapid and repetitive way the encoded evolution frequencies, mapping them as delays in the formation of constructive *k*-axis echoes. Various experimental examples were subsequently introduced to illustrate the generality of the method, while mathematical and spectroscopic details pertaining to the methodology were deferred to the last sections.

Even with the foundations of an ultrafast multidimensional NMR technique laid out, substantial research remains to be carried out to enable the routine use of this technology in single-scan 2D and in accelerated 3D NMR acquisitions. We believe that a particularly important factor in enabling the routine implementation of these experiments will be the development of suitable hardware, as it is clear that, although acceptable 2D spectra can often be collected with the hardware available in modern instruments for executing gradient-enhanced spectroscopy, significant gains remain to be reaped from the development of customized probehead equipment. Among other features, such equipment should include stronger gradients, faster switching times, a higher assembly rigidity, and, whenever possible, larger sample volumes. As for additional progress regarding more fundamental aspects of single-scan multidimensional NMR, it is to be noted that, despite this manuscript's length, the description that was here made of the progress in this area is only partial. For the sake of consistency, our attention was focused on the basic refocusing processes and potential artifacts arising in the methodology; yet several other interesting issues remain to be addressed. These include the incorporation of alternative excitation modalities, the utilization of shaped field gradients, the reliance on multiple orthogonal field gradients, and S/N enhancement possibilities that exploit the rapid sampling character of the experiments. Additional accounts describing these various features are being readied for publication. In view of the promise held by this protocol, it is also to be expected that other, independent contributions will follow.

Acknowledgment. We thank Mr. Ilija Uzelac (K. Kupcinet 2002 Summer School, Weizmann Institute) for assistance in writing the spin propagation program that was used during the course of this work, Dr. Eriks Kupce (Varian Ltd., Oxford) for assistance in recording the spectra shown in Figure 1, as well as Mr. Yoav Shrot (Weizmann Institute) for helpful discussions. A.L. is also grateful to the Feinberg Graduate School of The Weizmann Institute for an Anne Stone fellowship. This work was supported by the Philip M. Klutznick Fund for Research.

(36) Stephenson, D. S. *Prog. Nucl. Magn. Reson. Spectrosc.* **1988**, *20*, 515.
(37) Mandelshtam, V. A.; Taylor, H. S.; Shaka, A. J. *J. Magn. Reson.* **1998**, *133*, 304.
(38) Kim, S.; Szyperski, T. *J. Am. Chem. Soc.* **2003**, *125*, 1385.
(39) Kupce, E.; Freeman, R. *J. Magn. Reson.* **2003**, in press.

Appendix: Peak Intensities along the Indirect *k*-Domain

The $A(k)$ function introduced in eq 13 accounts for the refocusing/defocusing processes that magnetizations within the individual slices excited throughout the experiment will experience as a function of $k = \gamma_a \int_0^t G_a(t')\,dt'$. We state in this Article that, for the simple kind of excitation pulses considered in this study, these envelopes weighing the peaks observed along the indirect ν_1-domain are identical in shape to the rf pulses used in the selective excitation. We give here a justification for such a relation.

As all of the rf pulses employed throughout the excitation protocol possess the same shape, a unique envelope will characterize the rephasing/dephasing behavior of all spin-packets belonging to the various slices that are excited. Using the text's nomenclature, we found that this implies that a common $A(k)/N_1$ function will end up multiplying all $\{F_j\}_{j=0,N_1-1}$ magnetizations. To calculate this function, we shall assume that each individual slice in the sample is affected by only a single pulse; that is, no overlap arises between the excitation regions of consecutive pulses. We can focus then on the action of a particular pulse and compute its effects within the respective rotating frame of the slice on which it acts. The rf pulse in this frame can be simply expressed as $B_1(t) = B_1^o E(t)$, with B_1^o as the pulse's intensity, and $E(t)$ as an amplitude-modulated shape that extends between times $t = -T_p/2$ and $t = T_p/2$. In the linear regime approximation, which has been shown to yield relevant predictions even when the $dM_z/dt = 0$ condition it requires is not strictly fulfilled,[24] the transverse magnetization excited by this selective pulse can be expressed as

$$M_+(\delta z) = \gamma B_1^o \frac{M_o}{L} e^{-i\gamma_e G_e \delta z T_p/2} \int_{-T_p/2}^{T_p/2} E(t) e^{i\gamma_e G_e \delta z t}\,dt \quad \text{(A1)}$$

where M_o is the site's overall magnetization, L is the sample length, and δz reflects a spin's position within the slice. Because we are assuming that $E(t)$ is null for $t < -T_p/2$ and $t > T_p/2$, the integration limits in eq A1 can be replaced by $-\infty$ and $+\infty$, resulting in an equation which connects a slice's magnetization profile with the FT of the pulse's envelop. Disregarding all potential internal and external evolution frequencies that are accounted for by the remaining components making up F_j (cf., eq 6), the signal amplitude generated by this spin-packet during the course of the G_a-driven acquisition can then be written as

$$\frac{A(k)}{N} \approx \int_{\text{slice}} e^{-ik\delta z} M_+(\delta z)\,d(\delta z) \quad \text{(A2)}$$

The signal amplitude has now clearly become a function of the acquisition variable k. Because we had assumed that the effects of an excitation pulse were confined to one particular slice, it follows that $M_+(\delta z)$ in eq A1 is null beyond the slice, and the limits of integration in eq A2 can once again be assumed to range between $\pm\infty$. Taking the expression for $M_+(\delta z)$ from eq A1, inserting it into eq A2, and reversing the order of the integration then leads to

$$A(k) \approx \gamma B_1^o M_o \int_{-\infty}^{+\infty} E(t)\left[\int_{-\infty}^{+\infty} e^{i(\gamma_e G_e T_p/2 - k - \gamma_e G_e t)\delta z}\,d(\delta z)\right] dt \quad \text{(A3a)}$$

$$\approx \gamma B_1^o M_o \int_{-\infty}^{+\infty} E(t) \cdot \delta(\gamma_e G_e T_p/2 - k - \gamma_e G_e t) \cdot dt \quad \text{(A3b)}$$

$$\approx \gamma B_1^o M_o E\left(\frac{\gamma_e G_e T_p/2 - k}{\gamma_e G_e}\right) \quad \text{(A3c)}$$

The proportionality that results between $A(k)$ and γB_1^o is a consequence of pursuing the linear approximation and is thus not really relevant. On the other hand eq A3c predicts that, shapewise, the $A(k)$ function will match the profile of the rf used in the spins excitation yet centered (in wavenumber units) at $\gamma_e G_e T_p/2$. This is again a reflection of the Fourier transform's self-reciprocal character, as the procedure was used once to derive $M_+(\delta z)$ from $E(t)$ and then employed again to derive $A(k)$ from $M_+(\delta z)$. Despite the limitations involved in the linear approximation used throughout this derivation, numerical simulations reveal the correctness of this prediction over a large range of meaningful conditions. These include situations where a significant degree of overlap arises between the rf pulses used to excite adjacent slices. Further discussions on the consequences of this equation will be presented in a future publication.

JA030055B